Quantifying the Role of Transition Metal Electrodeposition in the Cathodic Activation of Corroding Magnesium

E. Michailidou, [z] **H. N. McMurray,*** **and G. Williams**

Materials Research Centre, College of Engineering, Swansea University, Bay Campus, Crymlyn Burrows, Swansea SA1 8EN, United Kingdom

High purity (80 ppm iron) magnesium immersed in aqueous sodium chloride solution exhibits a filiform pattern of localized corrosion in which hydrogen is evolved at local (filament head) and remote (filament tail and uncorroded surface) cathode sites. Transition metal cations in solution are shown to significantly accelerate rates of corrosion, principally by activating (catalyzing) the remote cathode sites. The degree of activation is cation concentration dependent and efficiency increases in the order $Mn^{2+} < Fe^{2+} < Zn^{2+} < Cu^{2+}$. It is proposed that activation occurs as a result of transition metal electrodeposition through a displacement reaction. It is also shown that precipitation of insoluble transition metal (hydr)oxides through time-dependent cation hydrolysis competes with, and reduces the efficiency of, electrodeposition-induced cathodic activation.

 [DOI: 10.1149/2.0251805jes]

Manuscript submitted January 9, 2018; revised manuscript received March 8, 2018. Published March 15, 2018. This was Paper 1205 presented at the Honolulu, Hawaii, Meeting of the Society, October 2–7, 2016.

It has been shown elsewhere that magnesium and magnesium alloys typically follow a corrosion behavior in which the dissolution of magnesium results in a surface which exhibits enhanced activity for the cathodic hydrogen evolution reaction (HER).[1–5] It has also been shown that this effect can be produced when magnesium dissolves through anodic polarization.[1,3,5–8] Furthermore, it has been proposed that the surface enrichment in trace transition metals, such as Cu and Fe, contribute to enhanced cathodic activity in corroding magnesium.[1,5,9–15] Such transition metals inherently possess a considerably higher electrocatalytic activity for the HER, Equations 1–3, than does magnesium.[13] Calculations based on Density Functional Theory (DFT) have shown that the re-combination of surface adsorbed hydrogen atoms (Eq. 2) is the rate-limiting step on pure magnesium.[16] Conversely, it has been argued that (under the alkaline conditions that tend to prevail during active magnesium corrosion) the desorption of hydrogen on transition metals occurs via a Heyrovsky step (Eq. 3) and the availability of this alternative pathway is one of the factors which facilitates transition metal electrocatalysis of the HER.[15]

$$\text{Volmer step} \qquad H_2O + e^- \rightarrow H_{ads} + OH^- \qquad [1]$$

$$\text{Tafel step} \qquad 2H_{ads} \rightarrow H_2 \qquad [2]$$

$$\text{Heyrovsky step} \qquad H_2O + H_{ads} + e^- \rightarrow H_2 + OH^- \qquad [3]$$

where H_{ads} is a surface adsorbed hydrogen atom.

Magnesium of commercial purity and magnesium alloys typically incorporate a variety of transition metals which are either added intentionally to modify properties or occur as trace impurities. Examples of such alloying elements or impurities include iron, zinc, copper and manganese. These elements may not be homogeneously distributed within the magnesium matrix and frequently exist as distinct particles of sub-micron size.[17] For example, it has been shown that iron occurs as grain boundary segregates in 99.9% Mg.[5] Furthermore, it has been argued that such particles might reasonably be expected to act as local cathodes.[1,5,6,12–14,17] The mechanism through which they might contribute to the cathodic activation of corroding magnesium is not yet fully understood but several possible mechanisms have been proposed. These include: i) transition metal particles in electrical contact with the Mg matrix accumulating at the Mg/solution interface as the Mg matrix corrodes, ii) transition metal particles becoming electrically separated from the Mg matrix (by ejection into solution or entrapment in Mg-rich corrosion product), corroding with the release of the ions and these ions electrodepositing onto the Mg surface in an electrochemical displacement reaction (in which anodically dissolving Mg provides the electronic current for cathodic transition metal ion reduction) and iii) transition metal ions released as in ii) becoming incorporated in (or doping) the Mg (hydr)oxide film at the Mg/solution interface and rendering it more conductive or electrocatalytically active.[1,5,7,14,15]

Once electrically isolated from the magnesium matrix transition metal rich particles are likely to corrode rapidly releasing transition metal ions into solution. For example, the non-faradaic release of copper ions has been demonstrated in the case of AZ91 magnesium alloy corroding in aerated aqueous sodium chloride.[18] Such ions could diffuse away from the magnesium surface and play no further role. Alternatively, they could undergo hydrolysis and precipitate as transition metal (hydr)oxides. However, they could also diffuse (or migrate) to the magnesium surface and cathodically electrodeposit through a displacement reaction and it is this electrodeposition process that could contribute to cathodic activation of HER.[5,18] In the case of iron released from grain boundary segregate electrically separated from the matrix it has been shown that iron (re)deposition occurs preferentially on the "clear" uncorroded magnesium surface.[5] Furthermore, the presence in solution of iron complexing agents can strongly limit hydrogen evolution on corroding magnesium and it has been argued that this effect arises as result of iron sequestration preventing the redeposition process.[14,15]

The present paper aims to quantify the effect that transition metal ions have on the cathodic activation of corroding magnesium when added to solution in a known concentration. The metal ions selected for this study are the Fe^{2+}, Cu^{2+}, Zn^{2+} and Mn^{2+} ions as the corresponding metals commonly exist within the bulk composition of commercially important magnesium alloy, such as the AZ series, either intentionally as alloying elements or unintentionally as impurities. The higher oxidation state of iron (Fe^{3+}) was not used because of the marked acidity and corresponding hydrolytic instability of the Fe^{3+} aquocation. Two types of experiments have been performed. In the first, known concentrations of transition metal cations were established by dissolving an appropriate metal salt in the experimental electrolyte. In the second, known quantities of the solid metal salt were dropped directly onto the magnesium surface prior to electrolyte immersion. In all cases the rate of magnesium corrosion (Reaction 4) was determined by following volumetrically the accompanying evolution of hydrogen gas (Reaction 5).

$$Mg \rightarrow Mg^{2+}_{(aq)} + 2e^- \qquad [4]$$

$$2e^- + 2H_2O \rightarrow H_{2\,(g)} + 2OH^-_{(aq)} \qquad [5]$$

*Electrochemical Society Member.
[z]E-mail: emmamichailidou@gmail.com

Experimental

Materials.—Magnesium samples of high purity (<80 ppm Fe) were provided as a gift by Prof. A. Atrens (University of Queensland) and were cut into 3 cm square coupons of 0.5 cm thickness. The sample surface was prepared using silicon carbide polishing pads (Buehler CarbiMet) with ethanol used as lubricant during the process. The polishing order was ascending from grit 320 (P400) to grit 1000 (P2500) with the samples cleaned with detergent solution, rinsed with distilled water followed by ethanol at the end of the process. All the chemicals used were of analytical grade and provided by the Sigma-Aldrich Chemical Company. All glassware equipment was cleaned thoroughly using 2 M HCl (aq) followed by rinsing in distilled water.

Methods.—Rates of hydrogen gas evolution from corroding magnesium were determined volumetrically method. Abraded magnesium samples were covered with 90 μm thick extruded PTFE 5490 tape (3 M Ltd) leaving exposed a square area of 10 × 10 mm. Further PTFE tape strips were used in order to secure the sample on the petri dish. A 10 ml ± 0.02 ml conically ended burette was then placed on top of the sample at a minimal distance so that the exposed area was fully covered by the conical end of the burette, limiting the possibility of the evolved hydrogen gas escaping the burette tube. Freshly prepared electrolyte was poured into the petri dish and with the aid of a syringe the electrolyte was pulled upwards through the burette tube up to its maximum point. The burette valve was closed and the electrolyte volume reduced by the evolved H_2 gas was recorded at regular intervals. The salts $CuSO_4$, $FeCl_2$, $ZnSO_4$ and $MnCl_2$ were used as a source of transition metal cations. In one series of experiments, the metal salts were dissolved in distilled water and further diluted in 0.86 M NaCl aqueous solution at concentrations ranging from 10^{-6} M to 8×10^{-3} M. In a second series of experiments, the metal salts were placed in solid form (ranging from 5 mg to 50 mg) directly on to the Mg surface prior to the introduction of 0.86 M aqueous NaCl electrolyte. The pH of aqueous NaCl/transition metal salt solutions fell in the range pH 5.5 – pH 6.5.

Characterization of localized corrosion behavior in the presence and absence of transition metal salt additions was carried out using a Scanning Vibrating Electrode Technique (SVET). A full description of the SVET instrumentation used here, along with details on the calibration method, are given elsewhere.[4] SVET measurements were carried out using a probe consisting of a platinum wire sealed within a glass rod, forming a platinum micro-disc electrode of 125 μm diameter at the probe tip. Prior to its use, the probe tip was abraded with a silicon carbide paper of 1200 grit and was immersed in 2 M HCl followed by rinsing with distilled water. Magnesium samples were covered with PTFE tape leaving exposed a square area of 5 × 5 mm and were subsequently placed, face up on a Perspex levelling stage within a 2.5 L capacity Perspex tank. The probe tip was held vertically at a 100 μm distance from the exposed surface of the sample. Various transition metal salts, at a 10^{-4} M concentration, were added to the 0.86 M NaCl aqueous solution used as the electrolyte and scanning of the sample was immediately initiated following specimen immersion. Scanning was performed at regular intervals of ca. 8 min for up three hours, producing a series of SVET-derived current density maps.

The corrosion of pure magnesium was also examined in-situ via time-lapse optical microscopy[19] to investigate the influence of transition metals on the visual appearance of propagating filament-like corrosion features, with particular emphasis on the principal sites of visible hydrogen evolution. The sample under investigation was covered with PTFE tape leaving a 1 mm diameter circular area exposed. The sample was secured to the base of the petri dish using an arrangement of double-sided foam tape and PTFE tape. A Meiji Techinco optical microscope was used to observe the sample. Contamination and damage of the optical lens was avoided by using a submersible cap with a thin glass window area. The petri dish was filled with 250 ml of freshly prepared electrolyte, covering the sample. The optical focus was adjusted so that clear in-situ images of the sample could be taken. Digital images of the exposed sample area were taken every 30 sec for a time period of three hours using the time-lapse function incorporated on the Infinity I camera (Lumera Corporation) attached to the microscope lens. The photographic images were analyzed using Adobe Photoshop CS5. Post corrosion scanning electrode microscope (SEM) images of the magnesium surface and energy dispersive X-ray spectroscopy (EDX) maps were acquired using a Hitachi TM8000 SEM in electron backscatter mode.

Results and Discussion

Kinetics of hydrogen gas evolution.—The volumes of hydrogen produced as the cathodic product of filiform-like corrosion in the presence and absence of added transition metal ions of various type and concentration are plotted as a function of time in Figure 1. In all cases, the volume vs time curves exhibit an approximately linear behavior, except for 8×10^{-3} M $FeCl_2$, in which a time-dependent decrease in H_2 evolution rate is observed. The approximate linearity, and metal ion concentration dependence, observed in the majority of cases indicates that: a) the presence of transition metal cation in solution accelerates the rate of magnesium corrosion and hydrogen evolution, b) the accelerating effect increases as the transition metal cation concentration increases, c) the accelerating effect is 'non-accumulative', that is to say it does not increase (or build up) with time and d) the magnitude of the effect is strongly dependent on the identity of the cation. The accelerating effect is summarized in Figure 2 which shows H_2 evolution rates calculated from the slopes of the various linear H_2 evolution curves as a function of transition metal concentration and identity (in the case of 8×10^{-3} M $FeCl_2$ the time-averaged rate is used). Figure 2 shows that H_2 evolution rates increase by a factor of up to 10 as transition metal ion concentration is increased from zero to 8×10^{-3} M and that the efficiency of transition metal ions in producing this effect increases in the order $Mn^{2+} < Zn^{2+} \approx Fe^{2+} < Cu^{2+}$ (Figure 2). However, it was observed by eye that precipitates of insoluble, colored, transition metal (hydr)oxides were formed in the course of the H_2 evolution experiments. Hydroxide precipitation and cation depletion is likely to be a factor limiting the ability of transition metal cations dissolved in bulk solution to accelerate of H_2 evolution kinetics. It is also a possible cause of the non-linear H_2 evolution kinetics seen the case of higher concentrations of Fe^{2+}, as will be discussed further below.

The initial pH range employed in our experiments (pH 5.5–6.5) is such that the various transition metal exhibit reasonable hydrolytic stability over a period of hours. However, in the interests of making our results as relevant as possible to typical conditions of magnesium corrosion a pH buffer was not used. When magnesium corrodes in unbuffered electrolyte solution pH rapidly increases due to OH^- production through Reaction 5. As corrosion proceeds the precipitation of magnesium hydroxide [$Mg(OH)_2$] (solubility product $K_s = 5.61 \times 10^{-12}$ M^3)[20] tends to stabilize pH in the region pH10-11.[21–23] Under these conditions, hydrolysis of transition metal aquocations and the resulting precipitation of insoluble, electrically non-conducting, metal hydroxides is likely to be an important process competing with, and reducing the efficiency of, metal cation as a process producing cathodic activation at the magnesium (metal) surface. The relative ease of cation hydrolysis is expected to follow the thermodynamic tendency indicated by the hydrolysis coefficients (pK_a values) associated with the various transition metal aquocations. Hydrolysis of polyvalent cations is a stepwise process; however, as a rule of thumb, the onset of metal hydroxide precipitation is anticipated to occur when solution pH becomes greater than the first hydrolysis coefficient of the relevant metal aquo cation (pK_{a1}), values of which are given in Table I. In the case of $[Fe(H_2O)_6]^{2+}$ the problem of hydrolysis is likely to be exacerbated by the tendency to undergo aerobic oxidation to $[Fe(H_2O)_6]^{3+}$ via Reaction 7. $[Fe(H_2O)_6]^{3+}$ is highly acidic (Table I) and will hydrolyse rapidly and quantitatively at pH 11. The marked deviation of linearity in Fig. 1b for $Fe^{2+} = 8 \times 10^{-3}$ M might therefore be explicable on the basis of competing

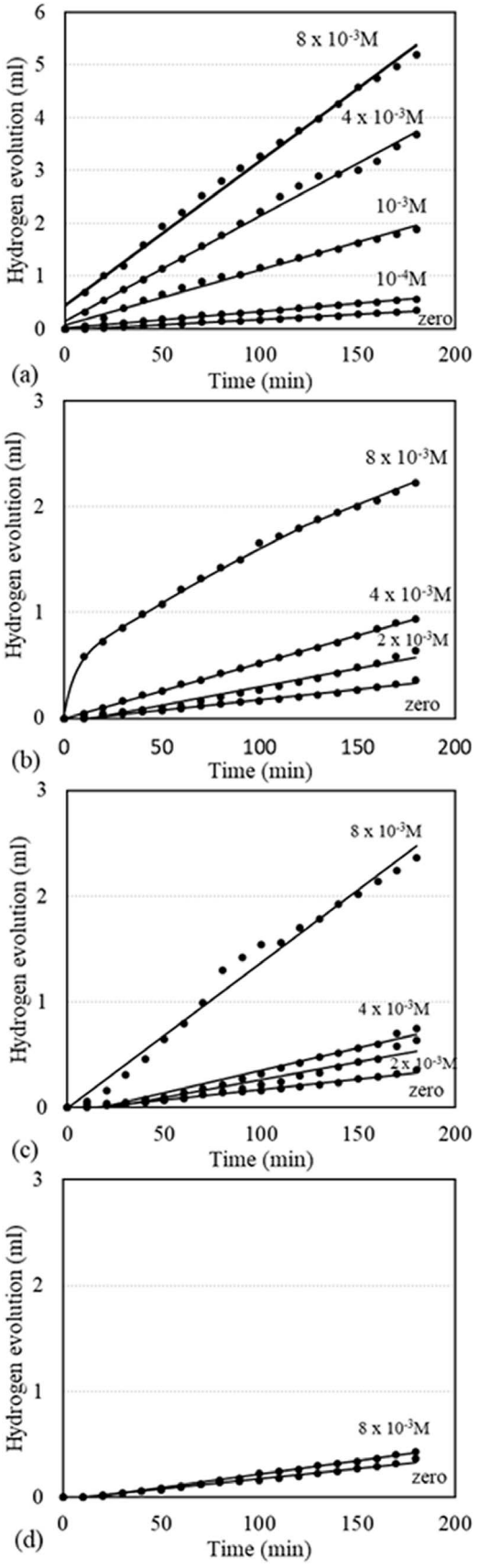

Figure 1. Plots of hydrogen volume vs time. The metal salts are diluted within 0.86 M aqueous NaCl prior to corrosion initiation. Metal salts key: (a) $CuSO_4$ (b) $FeCl_2$ (c) $ZnSO_4$ (d) $MnCl_2$. The labels indicate transition metal cation concentration in mol dm^{-3}.

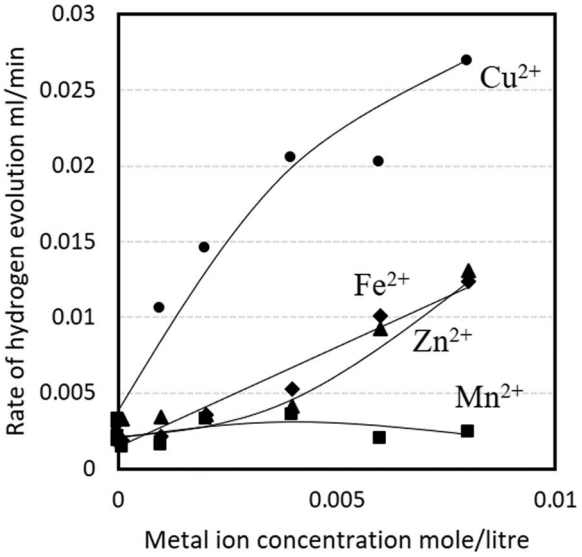

Figure 2. Rate of hydrogen evolution vs the metal salt concentration within the bulk electrolyte. Each point at graph represents the gradient of the hydrogen volume vs time plot for each corresponding metal cation concentration except for the case of 8 · 10-3 M $FeCl_2$ for which the average gradient has been taken over the experimental period (180 min).

oxidation and hydrolysis through Reactions 6 and 7.

$$\left[M(H_2O)_6\right]^{2+} \overset{pKa_1}{\rightarrow} \left[M(H_2O)_6\right]^{+} + H^{+} \quad [6]$$

$$4Fe^{2+} + O_2 + 2H_2O \rightarrow 4Fe^{3+} + 4OH^{-} \quad [7]$$

In order to estimate the influence of competing precipitation reactions a second set of volumetric H_2 evolution measurements were performed in which the solid, crystalline metal salts were deposited directly onto the exposed area of the magnesium sample. This approach was intended to minimize the effect of hydrolysis by reducing the ion mass transport (diffusion and/or migration) path length and the time during which hydrolysis could occur. Mohr's Salt ($Fe(NH_4)_2(SO_4)_2$) was used as the source of Fe^{2+} ions because the ammonia moieties associated with this compound are thought to help stabilize Fe^{2+} against becoming oxidized via Reaction 7.[24] The hydrogen volumes recorded for each quantity of the selected metal salts are plotted as a function of time in Fig. 3. In the majority of cases two distinctive phases where observed in the H_2 evolution kinetics. In an initial phase, which occurs over a period $\leq$ 30 min following salt deposition, H_2 evolution is initially high but decreases with time. In a final phase, H_2 evolution is slower and the H_2-volume-time curves become approximately linear, in a manner resembling those in Figure 4. Initial rates of H_2 evolution (Initial phase in Figure 3) are summarized for the various metal salt additions in Figure 4a. The later, more constant, rates of H_2 evolution (Final phase in Figure 3) are similarly summarized in Figure 4b. In both Figs. 4a and 4b the accelerating effect on H_2 evolution rate increases with the quantity of salt added. Furthermore, the efficiency

Table I. pKa_1 for the Selected Transition Metal Ions. Values Obtained from S.J. Hawkes.[26]

Metal Ion	pKa_1 at 25°C
Fe^{3+}	2.2
Cu^{2+}	7.5
Fe^{2+}	9.4
Mg^{2+}	11.2
Mn^{2+}	10.6
Zn^{2+}	9.0

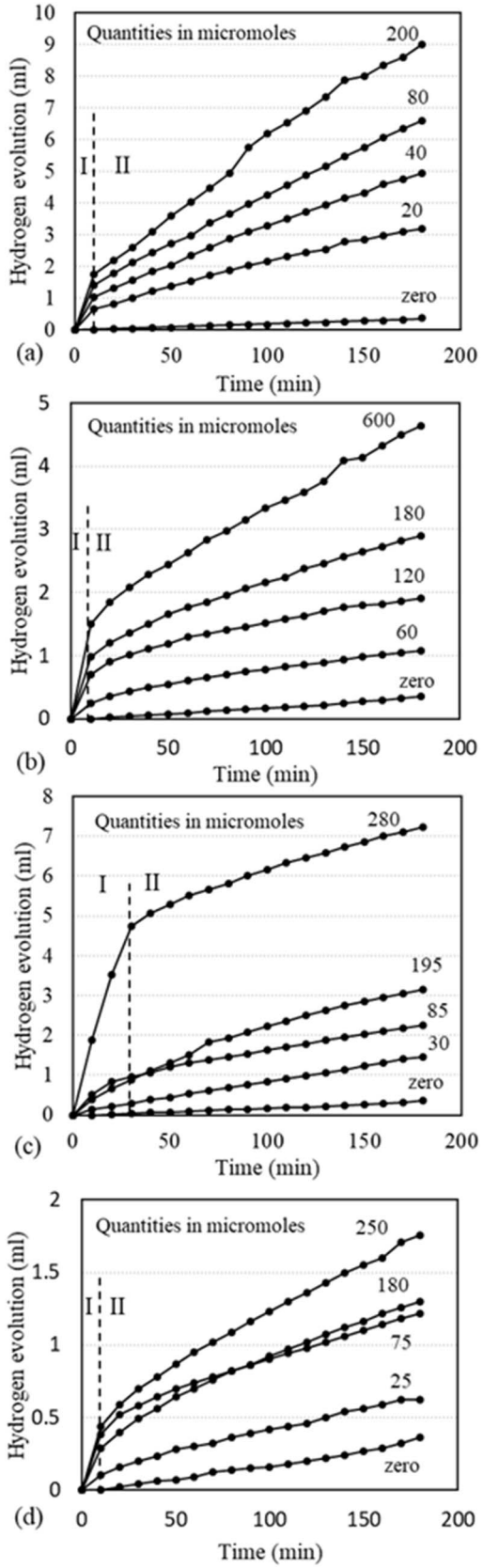

Figure 3. Plots of hydrogen volume vs time. The metal salts are diluted within 0.86 M aqueous NaCl prior to corrosion initiation. Metal salts solid on Mg surface key: (a) $CuSO_4(5H_2O)$ (b) $Fe(NH_4)_2(SO_4)_2(6H_2O)$ (c) $ZnSO_4(H_2O)$ (d) $MnCl_2(4H_2O)$. The labels indicate transition metal cation concentration. Phase I: rapid, initial H_2 evolution. Phase II: later, slower H_2 evolution. The labels indicate transition metal cation concentration in μmol.

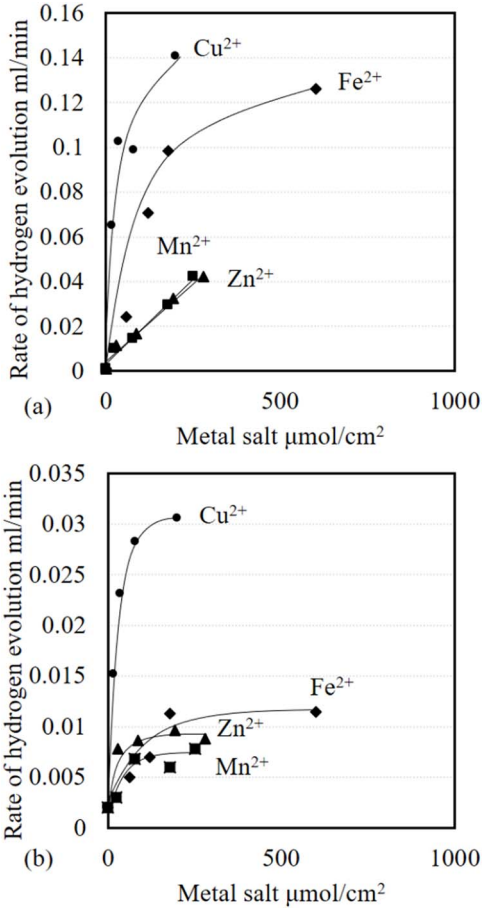

Figure 4. Phase I (a) and Phase II (b) rate of hydrogen evolution vs the quantity of metal salt dropped on the surface of magnesium. Each point at graph represents the average taken over time.

of acceleration depends strongly on the metal salt used and increases in the order $Mn^{2+} < Zn^{2+} \approx Fe^{2+} < Cu^{2+}$. A marked difference in efficiency is seen for Fe^{2+} additions in phase I and phase II of the H_2 evolution curve. As before, this can best be understood in terms of the redox instability of Fe^{2+} and the acidity (low pK_{a1}) of the resulting Fe^{3+} aquocation resulting in extensive cation hydrolysis during phase II.

A comparison of Figures 1 and 3 shows that the rates of hydrogen evolution in the initial phase of Figure 3 are considerably greater than those in Figure 1 and final phase of Figure 3, despite the quantity of transition metal salt present being similar in absolute terms. The most straightforward explanation for these results would be that the first (rapid) phase of the H_2 evolution in Figure 3 corresponds to a period where the solid transition metal salt is dissolving and a high concentration of transition metal aquocations is maintained at near Mg surface. In the second (slower) phase the transition metal salt has fully dissolved into the bulk electrolyte and the situation more closely resembles the conditions relevant to and discussed in the content of Figure 1. However, the possibility cannot be excluded that the high local concentration of transition metal aquocations evolved during the first phase might also lead to (aggressive) conditions of low local pH as a result of aquocation hydrolysis (as indicated by the pKa values in Table I). Whatever the exact mechanism, the much greater H_2 evolution rates observed in the initial phase help to confirm the hypothesis that the corrosion accelerating effect of the transition metal ions is likely to be much greater when the source of transition metal ion is local and close to the Mg surface. Under these circumstances high local transition metal ion concentration, short diffusion path lengths

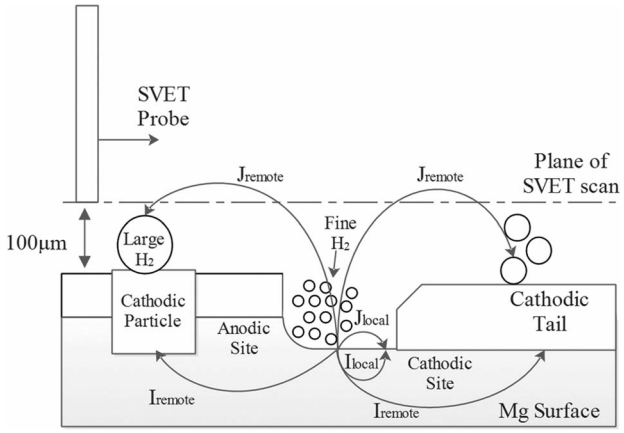

Figure 5. Schematic representation of the spatial resolution of the SVET plane of scan in relation with the localized anode and cathode site and the "remote" cathode sites occurring on the uncorroded magnesium surface and the filament tail.

and lack of time for competing hydrolysis reactions will maximize the efficiency of transition metal electrodeposition.

The approximately linear hydrogen evolution kinetics seen in Figure 1 and in the final phase of Figure 3 imply that any transition metal becoming electrodeposited onto the metallic surface of corroding magnesium does not do so in such a way that a time-dependent accumulation of electrodeposit results in a time-dependent increase in H_2 evolution rate. The observed kinetics require the extent of cathodic activation to depend upon the identity and concentration of the available transition metal cation but to rapidly become substantially time-independent. This scenario would be consistent with a steady-state hypothesis in which the (concentration dependent) rate of transition metal electrodeposition becomes equal to the rate of transition metal de-activation through overcoating with electrically insulating $Mg(OH)_2$. The solubility product (K_{sp}) of $Mg(OH)_2$ is 5.61×10^{-12} M^3[20] and the solubility of $Mg(OH)_2$ will be lowest where solution pH is highest, i.e. at the sites of highest cathodic activity producing the highest rates of Reaction 2.[11,17,25,26] Thus, surface sites becoming cathodically activated through transition metal electrodeposition would rapidly become deactivated. When the rate at which the cathodic site is formed equals the rate at which it is deactivated the effective cathodic area remains constant over time.

In-situ optical time-lapse microscopy.—The H_2 evolution experiments described above give no information on the location, size or shape of the sites associated with cathodic hydrogen evolution or how these are influenced by the addition of transition metal cations. However, it is well known that the corrosion of magnesium in aqueous chloride electrolytes is highly localized and that often more than one type (morphology and location) of hydrogen cathode is observed. It has been shown elsewhere that when magnesium samples are immersed in a near-neutral aqueous chloride electrolyte the onset of localized corrosion is not typically instantaneous.[27] Initially, a "pre-breakdown phase" is observed in which a generalized thickening of the surface oxide film is coupled to cathodic hydrogen evolution occurring at a relatively small number of (remote) cathodic sites, believed to arise from the local penetration of the oxide film by (inter)metallic impurity particles.[27,28] After a variable period of time the surface oxide breaks down and the onset of localized corrosion is observed, usually associated with the evolution of a large number of fine hydrogen bubbles at a (local) cathodic site at or near the magnesium dissolution front.[28] During the subsequent corrosion process hydrogen evolution continues to occur simultaneously at mixture of remote and local cathodic sites. A mechanistic scheme has been proposed in which the local cathodic sites act to "amplify" the cathodic current provided by the remote sites, as shown schematically in Figure 5.[28,29] As a result

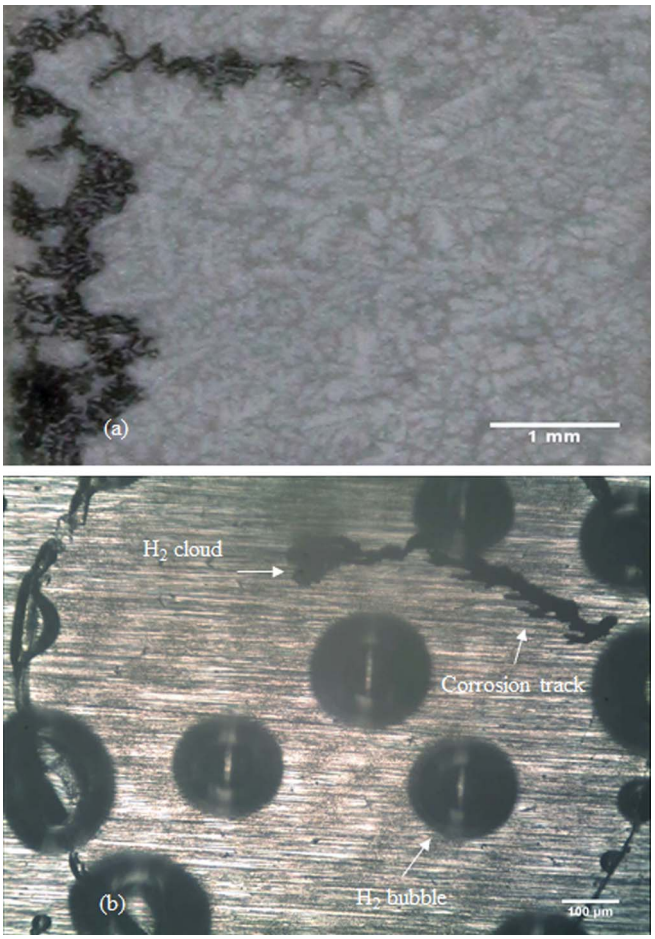

Figure 6. (a) Filiform-like corrosion on high purity magnesium (< 80 ppm Fe) after 180 min of immersion in 0.86 M aqueous NaCl, and (b) in-situ image of an active filament progressing along the bare magnesium surface after 12 min of immersion conditions in 0.86 M NaCl aqueous electrolyte.

the total cathodic current and rate of hydrogen evolution will be the sum of the remote current (I_{remote}) and local current (I_{local}), where the latter is related to HER at the corrosion front where Mg is actively dissolving.

With the aim of better determining the localization of corrosion related reactions in the presence and absence of added transition metal cations, a series of experiments were performed in which the corroding magnesium surface was observed using in-situ time-lapse optical microscopy. Optical microscopy cannot quantify the rate of electrochemical processes, however it does permit a precise localization of hydrogen evolution and a quantification of the lateral propagation velocity associated with localized corrosion features. Figure 6a shows the typical appearance of the Mg sample surface after immersion for 180 min in the absence of any added transition metal cation. The corroded region is seen as darkened area against the lighter uncorroded background. The shape of the corroded region is filamentary and reflects a filiform morphology of corrosive attack. Filiform or "filiform-like" corrosion is typical of "high purity" magnesium samples containing < 80 ppm iron immersed in 0.86 M NaCl.[3] It has been shown elsewhere that as iron content increases to 280 ppm Fe corrosion morphology in 0.86 M aqueous NaCl changes to produce "disk-like" features.[4] A higher resolution image, taken in-situ of a typical individual actively propagating corrosion filament, is given in Figure 6b. The cloud of fine bubbles observed at the filament head indicates that this is a significant (local) site of cathodic hydrogen evolution. There is no visible evidence of such fine hydrogen bubbles evolving along the filament tail. However, the physically large bubbles

seen evolving elsewhere on the sample surface are consistent with the presence of other, (remote), cathodic sites.

It should be noted that the very high rates of hydrogen evolution produced by higher concentrations of transition metal ion made recording legible images impossible. Consequently, a standard addition of 10^{-4} M transition metal was used for all the experiments reported here. At this concentration the acceleration of H_2 evolution rate was measurable but relatively limited: 55% for Cu^{2+}, 5% for Fe^{2+}, 60% for Zn^{2+} and zero for Mn^{2+}. When transition metal ions were added to the experimental electrolyte the mode of corrosive attack remained filamentary and the localization of visible hydrogen evolution remained substantially unchanged. Similarly, the velocity at which individual filaments were seen to advance over the magnesium surface (the rate of filament lengthening) did not appear to change significantly. However, the number of filaments becoming active typically increased (as will be shown later on). Figure 7 shows a series of images recorded for a typical corrosion filament when the experimental electrolyte contained 10^{-4} M $CuSO_4$. As in the case of Figure 6, a cloud of fine bubbles can be seen rising from the filament head but there is no indication that the presence of Cu^{2+} in solution has produced any persistent activation leading to visible hydrogen evolution in the filament tail. Again, the circular features appearing on the uncorroded Mg surface correspond to large bubbles of H_2 evolved at remote cathodic sites. The velocity of filament advance was determined by measuring the time-dependent filament length in successive time-lapse images. In so doing, care was taken to measure the true geometrical length of individual filaments, taking into account any changes in filament direction. Figure 8 shows filament length plotted versus time for filaments measured in the presence and absence transition metal ion addition. In all cases, filament length increases linearly with respect to time with a velocity of 1.39 ± 0.05 μm sec^{-1}. These linear propagation kinetics are entirely consistent with previous observations on Mg specimens of varying purity, as is the velocity of filament propagation.[30] However, no further insight could be obtained by optical microscopy and in order to further elucidate the effect of transition metal ions it became necessary to make spatially resolved current density measurements, as described in Scanning vibrating electrode technique section below.

SEM images and EDX elemental maps were acquired from a magnesium sample corroded in the presence of transition metal ions with the aim of better characterizing the morphology of corrosive attack, the distribution of corrosion products and the location of any transition metal deposition. Figures 9a–9d shows a series of backscatter SEM and EDX images obtained from a magnesium surface following 3 hours of exposure to 0.86 M aqueous NaCl electrolyte containing 8×10^{-3} M $CuSO_4$. After emersion the sample had been washed quickly with distilled water, then ethanol and dried in air. In the backscatter image, Figure 9a the filamentary corroded region appears as darkened area against the lighter uncorroded background. The corroded region has a granular appearance consistent with localized magnesium dissolution and the presence of a dried magnesium (hydr)oxide corrosion product. Close to the corroded region, but not necessarily associated with it, are a series of light regions (of high electron scattering efficiency) which vary between approximately 10 and 100 micron in diameter. The presence of an (hydr)oxide corrosion product in the corroded filament is confirmed in Figures 9b and 9d which show a local increase in the EDX counts for oxygen and a corresponded reduction in counts for magnesium, respectively. The distribution of copper is shown in Figure 9c. Copper is detectable over the whole sample surface and is not directly associated with the corroded region. However, the maximum copper counts are co-located with the light regions in the electron backscatter image, Figure 9a, implying that these are rich in either metallic copper or a copper containing compound. As such, Figure 9 is consistent with the notion that copper becomes deposited on the magnesium surface when this is corroding in the presence of aqueous Cu^{2+} cations. However, it must be recognized that EDX gives no information on the oxidation state of copper (i.e. whether or not the surface copper is the metallic product of cathodic electrodeposition) or the depth distribution of copper

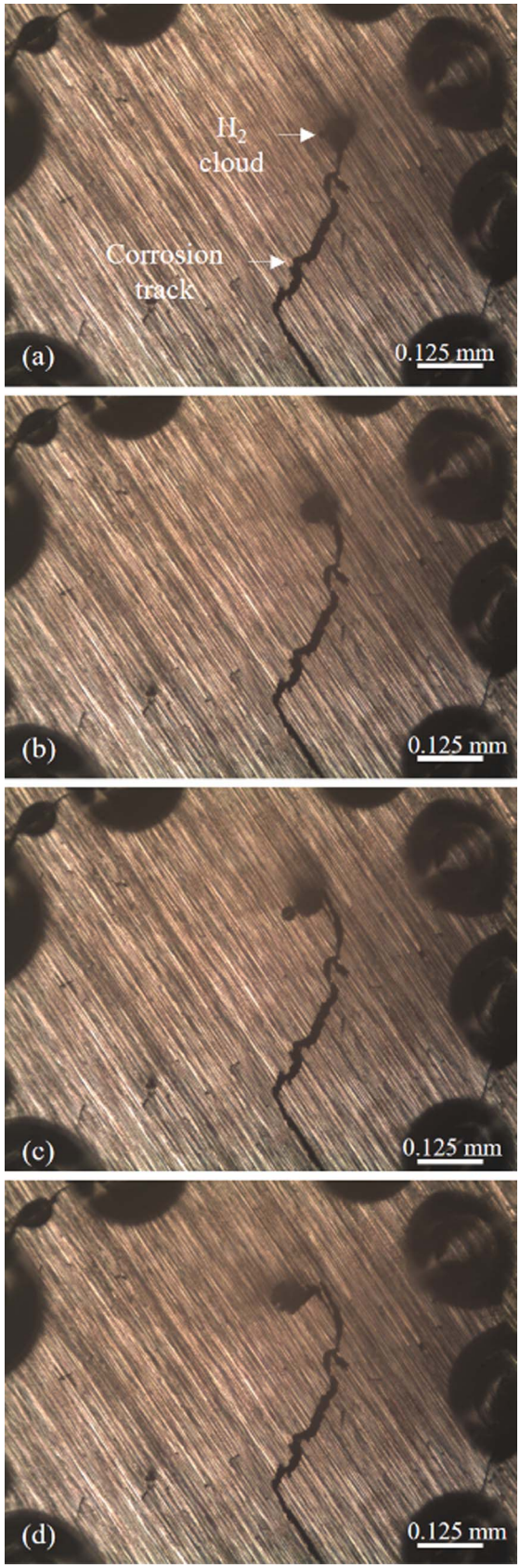

Figure 7. Photographic images taken during in-situ time-lapse microscopy. The photos illustrate the progression of a corroding filament on the bare Mg surface under immersion conditions in 10–4 M $CuSO_4$ contained 0.86 M NaCl aqueous electrolyte. Time key following immersion to electrolyte: (a) 360 sec, (b) 390 sec, (c) 420 sec, and (d) 450 sec.

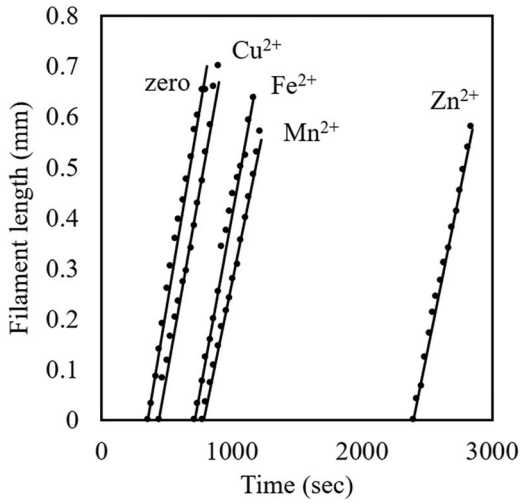

Figure 8. Filament length of corroding magnesium vs time for each selected metal cation showing the propagation of local anode on a pure magnesium surface immersed in 10–4 M $MnCl_2$ contained 0.86 M NaCl aqueous electrolyte.

(i.e. whether or not it lies in direct contact with metallic magnesium). To properly ascertain the oxidation state and depth distribution of transition metal-rich deposits will require further and detailed work.

Scanning vibrating electrode technique.—A sequence of SVET-derived current density maps, showing the normal (vertical) component of current density (j_z) over a single corrosion filament propagating on Mg immersed in 0.86 M NaCl (aq) without addition of transition metal ions is given in Figure 10. The leading edge of the filament head is a net anode which moves away from the site of filament initiation and leaves behind a tail exhibiting enhanced cathodic activity. Similar findings have been presented in several previous publications.[3,31] Line profiles of j_z vs distance constructed parallel with, and normal to, the direction of filament propagation at different immersion times are shown in Figures 11a and 11b, respectively. The j_z data in Figure 11a were taken along the axis a-a' indicated in Figure 10 and the data in Figure 11b were taken along the axis b-b'.

Figure 11a shows a substantially symmetrical peak in anodic j_z current density, located over the leading edge of the propagating filament, which moves from left to right as immersion time increases. The velocity of peak advance is 1.15 μm sec^{-1}, similar to the velocity of filament propagation (1.39 $\pm$ 0.05 μm sec^{-1}) measured from the time-lapse photographic data in Figure 7. The peak width at half maximum (whm) is constant at 250 μm and reflects the limiting lateral resolution of the SVET instrument rather than the physical size of the surface anode site. Isaacs has shown that SVET scanned over a point current source will record a whm of 1.532 h, where h is the scan height.[32] In our experiments h is 100 μm, implying a point-source whm of 153μm, but the diameter of the SVET probe microdisc is 100 μm so that the total whm will be approximately 250 μm. In Figure 11b the cathodic j_z distribution across the filament tail similarly exhibits a substantially time-independent whm. However, the whm value is now ~500 μm, twice than expected for a point source, so that the data in Figure 11b does to some extent reflect the physical diameter of the filament tail cathode. This is greater than the visible filament tail width of 20 μm seen in Figure 7 because the line b-b' lies at an angle to the axis of filament propagation.

Figure 11a shows that the peak j_z associated with the filament head anode increases from 90 A m^{-2} to 150 A m^{-2} as immersion times increases from 48 min to 84 min. The increased anodic current is balanced by the increasing area of enhanced cathodic j_z associated with the lengthening filament tail. However, Figure 11b shows that cathodic j_z values across the filament tail decrease over time, probably due to increased cathode pH resulting in a local precipitation of $Mg(OH)_2$. At first sight, the finding that the filament head is strongly

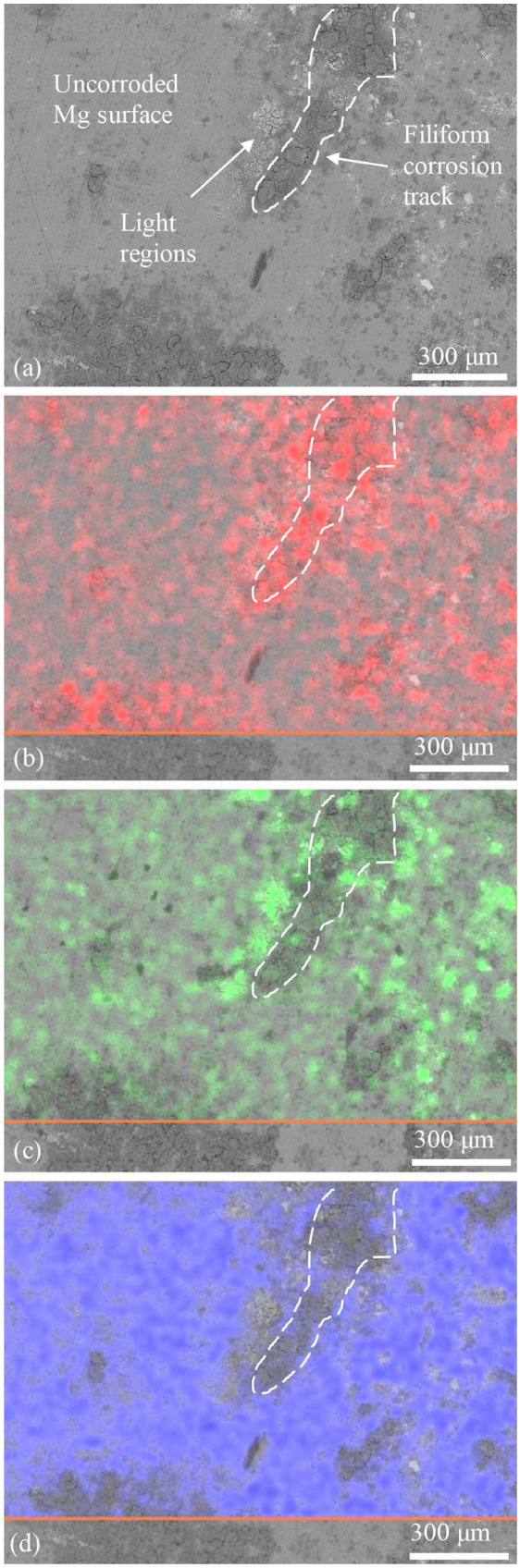

Figure 9. SEM/EDX elemental mapping of magnesium surface following exposure for 3 hours to $8 \cdot 10^{-3}$ M $CuSO_4$ containing 0.86 M aqueous NaCl electrolyte. Label key: (a) SEM image, (b) oxygen elemental map, (c) copper elemental map, and (d) magnesium elemental map. All images were taken at backscatter electron mode at 15 keV and 100x magnification.

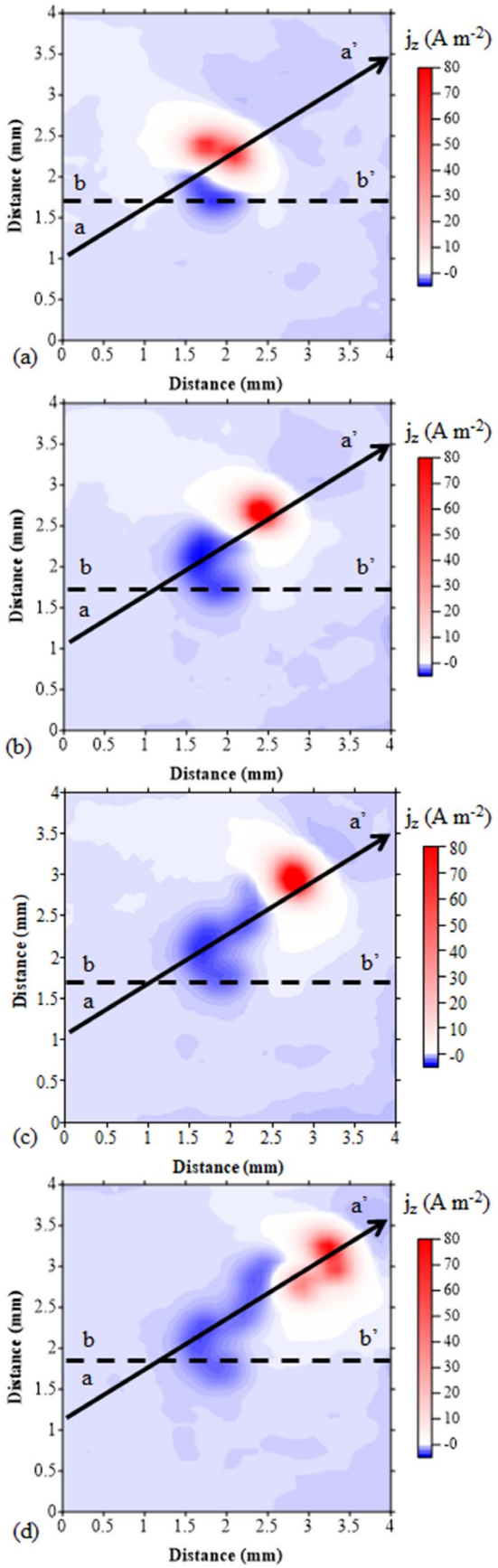

Figure 10. SVET-derived j_z surface maps showing the evolution of localized corrosion on a pure Mg (< 80 ppm Fe) surface after immersion in 0.86 M NaCl(aq) at pH 6.5 for (a) 48 min, (b) 62 min, (c) 69 min and (d) 84 min.

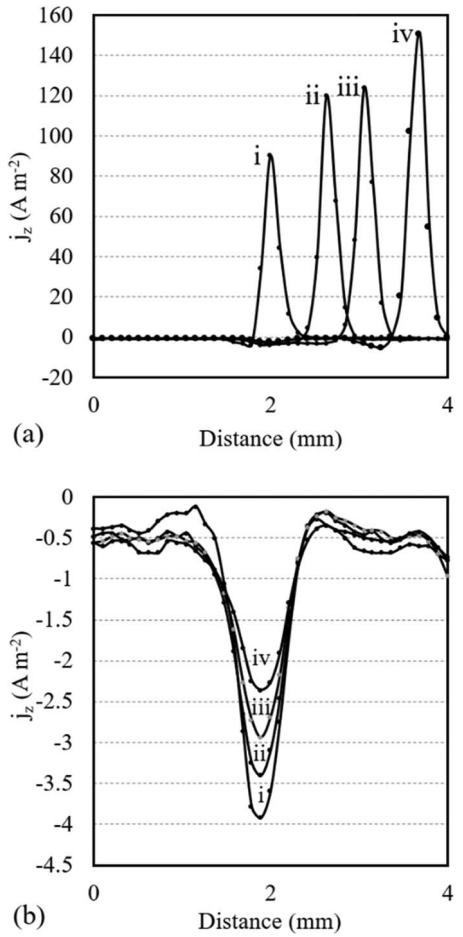

Figure 11. (a) SVET-derived current density (j_z) versus distance profiles taken along the length of a propagating corrosion filament (axis a-a' in Figure 2) and (b) over a local cathodic site (axis b-b' in Figure 2) on a pure magnesium surface immersed in 0.86 M NaCl aqueous electrolyte. Time Key: (i) 48 min, (ii) 62 min, (iii) 69 min, (iv) 84 min following immersion.

anodic in all the SVET data sets seems at odds with the observation of a co-located rising stream of hydrogen bubbles, as seen in Figure 6b. However, it must be remembered that SVET only determines the net (anodic-cathodic) j_z ionic current flux passing through the plane of scan.[33] This implies that, in order to be detected by SVET, the anodic source of current flux and the cathodic drain (on the corroding surface) must be physically separated by a distance (d) where $d \geq h$, the scan height. Under these circumstances the ionic flux loops linking anode to cathode through solution are likely to pass through the plane of scan. Conversely, when $d < h$ the ionic flux loops linking anode to cathode may be substantially completed beneath the plane of scan and SVET will not detect them efficiently or at all. It should be noted that it is the separation between the anode and cathode sites which determines their detectability and not their individual physical size. Any current source with a diameter significantly smaller than h but with a drain at $d > h$ will be detected as "point source", as described above.

Figure 5 shows schematically the spatial relationships between: the SVET plane of scan, the filament head anode site, the filament head (local) cathode site and (remote) cathode sites on the uncorroded magnesium surface and the filament tail. Figures 6 and 7 indicate that the local hydrogen cathode extends behind the front edge of the filament head (the site of anodic magnesium dissolution) a distance which is similar to the filament width (typically ~20 μm). This implies that the filament head anode and the local hydrogen cathode are much closer together than the SVET scan height (100 μm) with the

consequence that the current flux (J_{local}) balancing the local cathodic current contribution (I_{local}) will not be detected (or will be detected very inefficiently) by SVET. Conversely, the filament head anode and the remote hydrogen cathodes (sites on the (hydr)oxide covered) magnesium surface may be separated by a distance as great as the diameter of the exposed sample surface (~5 mm). Under these circumstances the remote ionic current flux (J_{remote}) balancing the remote cathodic current contribution (I_{remote}) will pass substantially through the plane of scan and be detected efficiently by SVET.

For the reasons given above, a numerical area integral of SVET derived cathodic current flux (J_{remote}) densities over the plane of scan, given by Equation 8 in which j_z is the current flux density along axis of probe vibration,[4] is expected to provide a good estimate of the I_{remote} contribution to the total cathodic current. This numerical area integral was performed using Surfer mapping software which employed linear interpolation, a version of the trapezium rule. The series of instantaneous I_{remote} values obtained from a series of in-situ SVET scans over a single corroding sample using Equation 9 may then be numerically integrated with respect to time using Equation 10 to calculate the time-dependent volume of H_2 gas ($V_{remote}(H_2)$) evolving at the remote sites of cathodic hydrogen evolution. In so doing it was assumed that I_{remote} remained constant between successive SVET scans, i.e. linear interpolation was not used. For magnesium corroding in the absence of added transition metal cation, the volumetrically determined V(H2) and the SVET derived $V_{remote}(H_2)$ are both plotted vs time in curves (i) and (ii) of Figure 12e respectively. A comparison of the two curves suggests that approximately one third of the total H_2 evolved over the experimental period does so at the remote cathode sites and two thirds at the local (filament head) cathodes. Curve (i) is approximately linear, showing only a slight positive deviation from linearity toward the end of the experimental period. A single straight line has been constructed through these data to estimate the total hydrogen evolution rate. Conversely, the slope of curve (ii) increases significantly over time. Two straight lines have been constructed as tangents to estimate the initial and final rate of remote H_2 evolution. It has been shown elsewhere that the slope of a H_2 volume vs time curve can be used to calculate the cathodic H_2 evolution current using Equation 11.[34] Table II shows the total current, I_T, value obtained from the slope of curve (i) in Figure 12 together with the I_{remote} values obtained from the initial and final slopes of curve (ii). Also shown in Table II are the current amplification factor (AF) values calculated using Equation 12. The values for I_{local} are derived by subtracting I_{remote} from I_T and are displayed in Table II.

$$I_{remote} = A \cdot J_{remote} \geq \int_0^x \int_0^y \left[J_{z(x,y)} > 0 \right] dx\, dy \quad [8]$$

$$\frac{dV_{remote}}{dt} = I_{remote} \cdot \frac{RT}{P} \cdot \frac{1}{2F} \quad [9]$$

$$V_{remote}(t) = \int_0^t I_{remote} \cdot \frac{RT}{P} \cdot \frac{1}{2F} \quad [10]$$

$$I_T = \frac{dV}{dt} \cdot \frac{P}{RT} \cdot 2F \quad [11]$$

$$AF = I_T / I_{remote} \quad [12]$$

The observation in Figure 12e and Table II that the remote H_2 evolution rate (and I_{remote}) increases with time whilst the total H_2 evolution rate (and I_T) is approximately constant implies that the local (filament head) H_2 cathode does not act simply to "amplify" the current coming from the remote H_2 cathode sites. Instead it would seem reasonable to propose that the local cathode sites and remote cathode site compete to some extent.

On this basis the above SVET was used to determine the effect of transition metal ions added to the corrosive electrolyte on the development of remote and local (filament head) hydrogen cathodic activity.

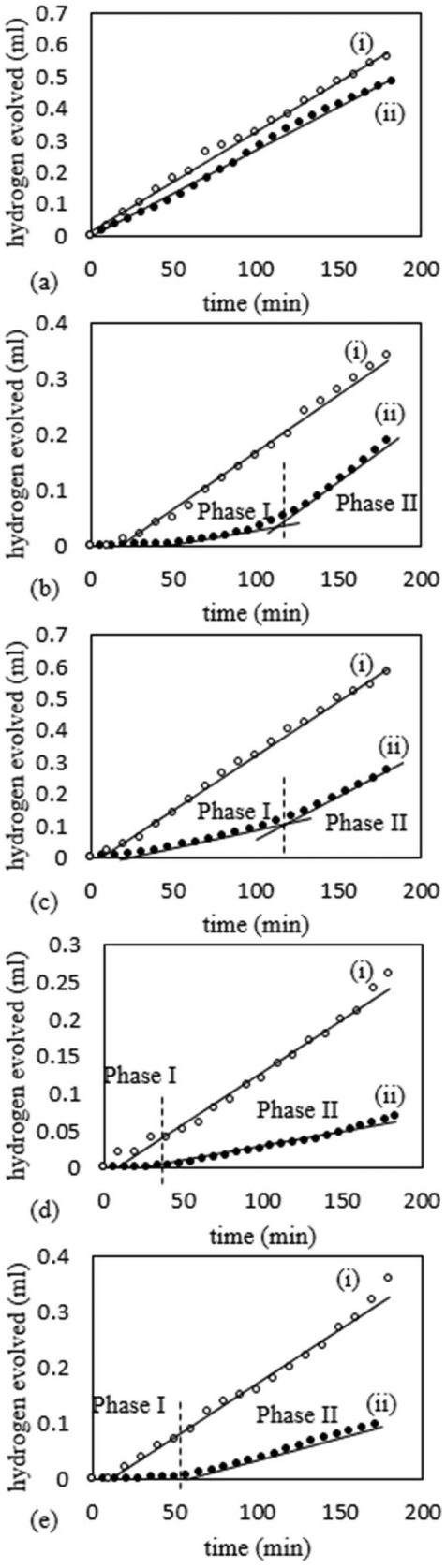

Figure 12. Comparison between the values obtained for hydrogen gas evolution during the volumetric measurements and SVET recording in the presence of 10^{-4} M of transition metal diluted within the bulk electrolyte for (A) $CuSO_4$ (B) $FeCl_2$ (C) $ZnSO_4$ (D) $MnCl_2$ and (E) 0.86 M aqueous NaCl. (●) SVET-derived H_2 evolution, (○) Volumetric H_2 evolution.

As in the case of time-lapse microscopy it was found that for higher concentrations transition metal the rapid rates of hydrogen evolution and corrosion product buildup made SVET measurement impossible. A standard addition of 10^{-4} M transition metal was therefore employed throughout. Typical SVET j_z distribution maps obtained in the presence of the various transition metal ion additions are shown in Figure 13. A comparison of Figure 12d with Figure 13d shows that 10^{-4} M Mn^{2+} ion addition has little effect on either the number or intensity of corrosion filaments. A similar comparison with Figures 13a, 13b and 13c show that Cu^{2+}, Fe^{2+} and Zn^{2+} additions all act to increase both the number and intensity of local anodic sites. The number of local anodes depends on the identity of the transition metal and increases in the order of $Mn^{2+} < Zn^{2+} < Fe^{2+} < Cu^{2+}$. However, it is also evident from Figures 13a–13c that the contrast in cathodic j_z between the filament tails and the uncorroded magnesium surface is lower in the presence of Cu^{2+}, Fe^{2+} and Zn^{2+} additions, to the extent that the filamentary nature of corrosive attack is no longer easily recognized in the SVET j_z maps.

For magnesium corroding in the presence of the added transition metal ions the volumetrically determined V (H_2) and the SVET derived $V_{remote}(H_2)$ calculated using Equations 9 and 10 are plotted vs time in curves (i) and (ii) (the respective curves) of Figures 11a–11d, respectively. Table II shows the I_T value obtained from the slope of curves (i) in together with the I_{remote} values obtained from the initial and final slopes of curves (ii). Also shown in Table II are the amplification factor (AF) values calculated from the various curve slopes using Equation 12. A comparison of Figure 12e with Figure 12d shows that that 10^{-4} M Mn^{2+} ion addition has little effect on the rate of remote H_2 evolution and this is reflected in the corresponding I_{remote} and AF values in Table II. However, a similar comparison with Figures 12a–12c shows that Cu^{2+}, Fe^{2+} and Zn^{2+} additions all act to increase the rate of remote H_2 evolution and that this effect increases with immersion time. The efficiency of transition metals in accelerating remote H_2 evolution increases in the order the $Mn^{2+} < Zn^{2+} < Fe^{2+} < Cu^{2+}$. The I_{local} and AF values shown in Table II reflect these changes and it may be seen that in the case of Zn^{2+}, $Fe^{2+}$and Cu^{2+} the AF value becomes ~1 at longer immersion times, implying that the majority of H_2 is being evolved at remote sites. Cu^{2+} is the most efficient of all in this respect and the corresponding AF remains ~1 for most of the experimental period.

The finding in Figures 11b–11c that remote H_2 evolution rates become approximately constant at longer immersion times again suggests a cathodic deactivation process competing with activation through transition metal electrodeposition leading to a steady state remote cathodic activity. Similarly, the finding that remote H_2 evolution rate can increase markedly with immersion time whilst total H_2 evolution rates remain nearly constant reinforces the notion that the remote H_2 cathode sites can compete with local cathode sites for the current released at the local anode. In highly conductive electrolyte (0.86 M NaCl) all the sites will experience a similar free corrosion potential and depolarization of the remote site (by transition metal electrodeposition and electrocatalytic activation) would also depolarize the local sites. If the local sites are not activated, or are more weakly activated, then depolarization will act to suppress local hydrogen evolution rates.

Conclusions

When high purity magnesium containing 80 ppm iron is immersed in 0.86 M aqueous NaCl without polarization in-situ optical micrography of growing corrosion filaments reveals two types and locations of hydrogen evolution. Remote cathode sites are located on the uncorroded magnesium surface and/or on the filiform tails. These produce coarse (100 s of microns diameter) hydrogen bubbles. Local cathode sites are located at the filiform head at, or immediately behind, the site of anodic magnesium dissolution. These produce a rapid stream of fine (microns diameter) hydrogen bubbles. The cathodic current contribution arising from remote cathode sites may be reasonably estimated using area-integrated cathodic current density data derived from SVET measurements. Conversely, the contribution from local

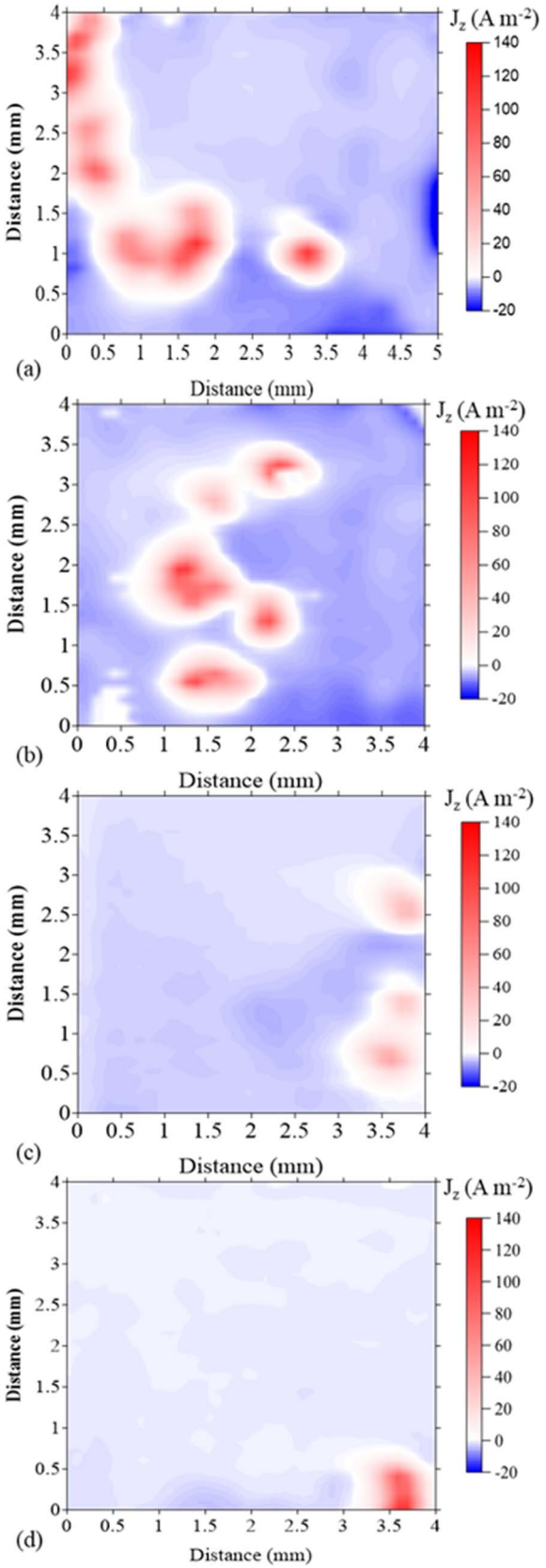

Figure 13. SVET-derived surface maps showing the normal current density (j_z) distribution on the exposed pure magnesium (80 ppm Fe) surface in the presence of 10^{-4} M of transition metal diluted within the bulk electrolyte 450 sec following corrosion initiation. Label key: (a) $CuSO_4$, (b) $FeCl_2$, (c) $ZnSO_4$, and (d) $MnCl_2$.

Table II. Amplification Factor in the Presence of 10^{-4} M of Transition Metal Diluted Within the Bulk Electrolyte. Standard deviation is 5%.

		I_{local} ($\mu A\ cm^{-2}$)		I_{remote} ($\mu A\ cm^{-2}$)		Amplification Factor	
Metal Ion	I_T ($\mu A\ cm^{-2}$)	Phase I	Phase II	Phase I	Phase II	Phase I	Phase II
Cu^{2+}	62.8	4.8120		58.007		1.083	
Fe^{2+}	39.3	23.7	26.3	15.6	0.3	2.522	0.619
Zn^{2+}	65.1	43.1	9.3	21.9	55.8	2.963	1.166
None	34.8	32.8	17.4	1.9	17.4	20.608	2.318
Mn^{2+}	29.2	27.9	18.7	1.1	10.5	24.427	2.788

cathode sites is not detected, or detected very inefficiently, by SVET. Total cathodic current may be estimated by numerical differentiation of the H_2 evolution volumetric curve. By comparing the SVET (remote) cathodic current data and H_2 (total) volumetric data it has been shown that approximately 30% of the cathodic current comes from the remote cathode sites and 70% (total-remote) from the local cathode sites.

When transition metal cations are dissolved in the corrosive electrolyte in concentrations up to 8×10^{-3} M rates of cathode hydrogen evolution increase by up to a factor of 5. The efficiency of cations in producing cathodic activation increases in the order $Mn^{2+} < Zn^{2+} < Fe^{2+} < Cu^{2+}$. The observed increase in cathodic activity is strongly associated with the remote cathode sites, such that when the solution contains 10^{-4} M Cu^{2+} > 90% of the total cathodic current comes from the remote sites. It is proposed that this effect results from the cathodic electrodeposition of transition metal on the intact (visibly uncorroded) magnesium surface and filiform tail areas. It is further proposed that the hydrolysis of transition metal cations in solutions alkalized through cathodic hydrogen evolution limits the efficiency of cathodic activation. This limitation would arise through the precipitation of solid transition metal hydroxides competing with the cathodic electrodeposition process. Although it should be noted that a porous hydroxide layer would still permit any underlying metallic electrodeposit to contribute to cathodic activity. When transition metal salt crystals are dropped directly onto the corroding magnesium surface initial rates of H_2 evolution are ~10 times greater that when a similar quantity is dissolved in the bulk solution. This finding is consistent with hydrolytic competition being reduced when transition metal cations are released in close proximity to the metal surface.

On the basis of the above it seems reasonable to conclude that ions released through the self-corrosion of, transition metal (rich) impurity particles becoming electrically separated from the magnesium matrix could contribute to corrosion-driven cathodic activation by diffusing (or migrating) back to the magnesium surface and becoming cathodically electrodeposited as native transition metal. However, the cathode sites affected would be the remote cathode sites on the uncorroded magnesium surface and on the filiform tails. There is no evidence to suggest that transition metal electrodeposition is responsible for the intense local H_2 cathodic activity at the filiform head. It therefore seems likely that the local cathode site comprises either magnesium itself or metallic impurities pre-existing in the magnesium matrix which become exposed as the original oxide-covered surface is removed by anodic magnesium dissolution.

List of Symbols

AF	Amplification Factor
d	Distance between well separated anode and cathode
h	SVET scan height
I_{local}	Current at local cathode
I_{remote}	Current at remote cathode
I_T	Total current
J_{remote}	Current flux at remote cathode
J_{local}	Current flux at local cathode
j_z	Normal component current density
P	Atmospheric pressure
R	Ideal gas constant
T	Temperature
V (H_2)	Total volume of H_2 derived volumetrically
V_{remote}(H_2)	SVET derived volume of H_2 at remote cathodes
whm	Width at half max

ORCID

E. Michailidou https://orcid.org/0000-0002-5437-2104

References

1. N. Birbilis, A. D. King, S. Thomas, G. S. Frankel, and J. R. Scully, *Electrochimica Acta*, **132**, 277 (2014).
2. G. S. Frankel, A. Samaniego, and N. Birbilis, *Corrosion Science*, **70**, 104 (2013).
3. G. Williams, N. Birbilis, and H. N. McMurray, *Electrochemistry Communications*, **36**, 1 (2013).
4. G. Williams and H. Neil McMurray, *Journal of The Electrochemical Society*, **155**(7), C340 (2008).
5. D. Mercier, J. Światowska, S. Zanna, A. Seyeux, and P. Marcus, *Journal of The Electrochemical Society*, **165**(2), C42 (2018).
6. S. Thomas, N. V. Medhekar, G. S. Frankel, and N. Birbilis, *Current Opinion in Solid State and Materials Science*, **19**(2), 85 (2015).
7. S. Fajardo, C. F. Glover, G. Williams, and G. S. Frankel, *Electrochimica Acta*, **212**, 510 (2016).
8. J. Światowska, P. Volovitch, and K. Ogle, *Corrosion Science*, **52**(7), 2372 (2010).
9. R. E. McNulty and J. D. Hanawalt, *Transactions of The Electrochemical Society*, **81**(1), 423 (1942).
10. J. D. Hanawalt, C. E. Nelson, and J. A. P. Medhekar, *Trans. AIME*, **147**, 273 (1942).
11. S. Fajardo and G. S. Frankel, *Electrochimica Acta*, **165**, 255 (2015).
12. T. Cain, S. B. Madden, N. Birbilis, and J. R. Scully, *Journal of The Electrochemical Society*, **162**(6), C228 (2015).
13. D. Lysne, S. Thomas, M. F. Hurley, and N. Birbilis, *Journal of The Electrochemical Society*, **162**(8), C396 (2015).
14. S. V. Lamaka, D. Höche, R. P. Petrauskas, C. Blawert, and M. L. Zheludkevich, *Electrochemistry Communications*, **62**, 5 (2016).
15. D. Hoche, C. Blawert, S. V. Lamaka, N. Scharnagl, C. Mendis, and M. L. Zheludkevich, *Physical Chemistry Chemical Physics*, **18**(2), 1279 (2016).
16. T. Vegge, *Physical Review B*, **70**(3), 035412 (2004).
17. M. Taheri, J. R. Kish, N. Birbilis, M. Danaie, E. A. McNally, and J. R. McDermid, *Electrochimica Acta*, **116**, 396 (2014).
18. J. Li, W. Sun, B. Hurley, A. A. Luo, and R. G. Buchheit, *Corrosion Science*, **112**, 760 (2016).
19. J. Sullivan, S. Mehraban, and J. Elvins, *Corrosion Science*, **53**(6), 2208 (2011).
20. N. A. Lange, *Lange's handbook of chemistry Norbert Adolph Lange*, New York: McGraw-Hill Education, New York (2013).
21. A. Pardo, M. C. Merino, A. E. Coy, R. Arrabal, F. Viejo, and E. Matykina, *Corrosion Science*, **50**(3), 823 (2008).
22. S. Virtanen, *Materials Science and Engineering: B*, **176**(20), 1600 (2011).
23. N. T. Kirkland, N. Birbilis, and M. P. Staiger, *Acta Biomaterialia*, **8**(3), 925 (2012).
24. D. Rickard and G. W. Luther, *Chemical Reviews*, **107**(2), 514 (2007).
25. J. Charles F. Baes and Robert E. Mesmer, *The hydrolysis of cations / Charles F. Baes, Robert E. Mesmer*, New York, London: Wiley, New York, London (1976).
26. S. J. Hawkes, *Journal of Chemical Education*, **73**(6), 516 (1996).
27. G. Williams, H. Ap Llwyd Dafydd, R. Subramanian, and H. N. McMurray, *CORROSION*, **73**(5), 471 (2017).
28. Y. Yang, F. Scenini, and M. Curioni, *Electrochimica Acta*, **198**, 174 (2016).
29. M. Curioni, J. M. Torrescano-Alvarez, Y. F. Yang, and F. Scenini, *Corrosion*, **73**(5), 463 (2016).
30. G. Williams, N. Birbilis, and H. N. McMurray, *Faraday Discussions*, **180**(0), 313 (2015).
31. K. D. Ralston, G. Williams, and N. Birbilis, *Corrosion*, **68**(6), 507 (2012).
32. H. S. Isaacs, *Journal of The Electrochemical Society*, **138**(3), 722 (1991).
33. G. Williams, A. J. Coleman, and H. N. McMurray, *Electrochimica Acta*, **55**(20), 5947 (2010).
34. S. Fajardo and G. S. Frankel, *Journal of The Electrochemical Society*, **162**(14), C693 (2015).